Anisotropic thermal conductivity in Li_2TiO_3 ceramic breeder materials

Megha Sanjeev[a], Mark R. Gilbert[b], Samuel T. Murphy[a,*]

[a] *Engineering Department, Lancaster University, Bailrigg, Lancashire, LA1 4YW, UK*
[b] *United Kingdom Atomic Energy Authority, Culham Centre for Fusion Energy, Culham Science Centre, Abingdon, Oxon, OX14 3DB, UK*

Abstract

The high anisotropy in the thermal conductivity of lithium metatitanate, Li_2TiO_3, is shown using the classical simulation method of Molecular Dynamics (MD). The thermal conductivity along the z-direction is markedly lower than that in x and y. This characteristic could be exploited in the fabrication of breeder blanket design to favourably adjust the thermal conductivity of Li_2TiO_3 by ensuring alignment along x or y. This work sets the foundation for investigating the effect of defects on the thermal conductivity of Li_2TiO_3, as anticipated to be formed during the lifetime of a breeder blanket.

1. Introduction

The potential for producing large quantities of low carbon energy has made the prospect of fuelling the world using fusion power an attractive concept. Fusion reactors use fuel in the form of two hydrogen isotopes, deuterium and tritium. Deuterium has a small natural abundance, sufficient to fuel a fleet of fusion reactors, and can be easily extracted from seawater. Naturally occurring tritium, however, is very rare, and must be bred during the operation of the reactor itself.

Tritium will be generated in the breeder blanket of a future fusion reactor [1]. In the plasma, the hydrogen isotopes, deuterium and tritium fuse together

*Corresponding author
Email address: samuel.murphy@lancaster.ac.uk (Samuel T. Murphy)

to produce an alpha particle and a neutron. The neutrons produced are not constrained by the magnetic field due to their lack of charge, therefore they escape the plasma and enter the blanket where they transmute lithium atoms to produce another alpha particle and tritium. This tritium is then extracted from the blanket, reprocessed and fed back into the plasma. The tritium reaction-creation life-cycle within fusion systems is illustrated in fig 1. The breeder blanket also serves as the channel for energy conversion in the reactor, transforming the kinetic energy of the neutrons into heat (along with producing an additional energy multiplication factor between 1.2 and 1.3 themselves via nuclear reactions [2]) to generate the electrical output of the reactor [3]. The overall electrical generating efficiency of a reactor is hence strongly tied to the effectiveness of heat transfer through the breeder blanket.

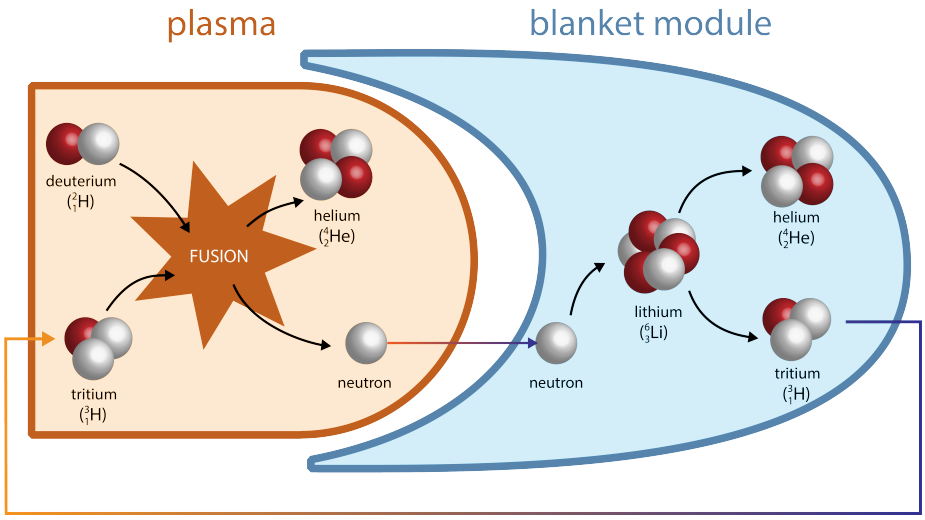

Figure 1: Schematic diagram of how tritium is bred inside a fusion reactor by using a breeding blanket containing lithium. The fusion reaction between the deuterium and tritium fuel produce an alpha particle and a high energy neutron, which escapes the plasma and enters the blanket module. These neutrons transmute lithium atoms in the blanket to produce an alpha particle and tritium. This tritium is extracted from the blanket and fed back into the plasma.

The final role of the blanket module is to act as a shield, preventing the high-

energy neutrons from damaging other components of the reactor, in particular the superconducting magnets used for the plasma confinement [2] and the vacuum vessel, which must last for the entire life of a reactor and is the primary safety barrier [4]. The breeder blanket must, therefore, withstand the extreme conditions inside the reactor, where materials are exposed to high-energy neutron irradiation and incorporation of transmutation products, which must not compromise the integrity or efficiency of the reactor, in order to achieve sustainable long-term fusion.

Numerous concepts for breeder blanket designs have been considered. The most common designs can be grouped into solid and liquid blanket concepts. Solid blanket designs involve the use of lithium ceramic breeders in the form of sintered pellets or slabs, or more commonly small pebbles. Using small pebbles of lithium ceramic ($\sim$ 0.5 - 2.0 mm diameter) limits the thermal stress in the breeder material and also prevents the pebbles being easily crushed in the blanket module. An example of a solid blanket design is the Helium-Cooled Pebble Bed (HCPB). Liquid blanket concepts, such as the Helium-Cooled Lithium Lead (HCLL) design, employ molten eutectic Pb-17Li as the breeder material [5, 2].

Of the candidate ceramic breeder materials, lithium-containing ceramics such as Li_4SiO_4, and Li_2TiO_3 are particularly attractive for their high Li density and good chemical stability [6]. Due to its higher lithium density, Li_4SiO_4 offers higher tritium breeding ratios, however Li_2TiO_3 has better chemical stability, good tritium release and low-activation characteristics [7], while also being insensitive to moisture [8]. Therefore, the best choice is not clear, as is evident in the differing approaches adopted by the international parties for development of test blanket modules for ITER [9].

Safe operation of a future reactor depends on understanding how properties of key functional materials change during operation. As such, it is important to understand how the thermal conductivity changes over time. The thermal conductivity of the blanket is a function of the thermal conductivity of the lithium ceramic pebbles themselves. Therefore, in this work we analyse the thermal conductivity of the lithium metatitanate, with the aim to describe the

thermal conductivity of the entire module.

The structure of β-Li_2TiO_3, the stable phase between 300 C - 1215 C [10], was first found by Lang [11] and subsequently refined by Kataoka *et al.* [12] using single crystal X-ray data. Li_2TiO_3 can be considered as a disordered rocksalt structure with alternating Li, O and $LiTi_2$ (111) planes described with the C2/c space group. An illustration of the unitcell is presented in figure 2. From this diagram of the unit cell, the complex layered crystal structure of Li_2TiO_3 is evident as is the distinct difference in each spatial direction, x, y, and z. Highlighted in the diagram are the three different layers in Li_2TiO_3, the lithium Li_6 layer, the oxygen O_6 layer and the mixed cation layer of Li_2Ti_4 [13]. This final layer forms a honeycomb structure in the xy-plane which can be stacked on top of each other in a number of different ways. This complex structure implies that physical properties in the material along each axis will be different.

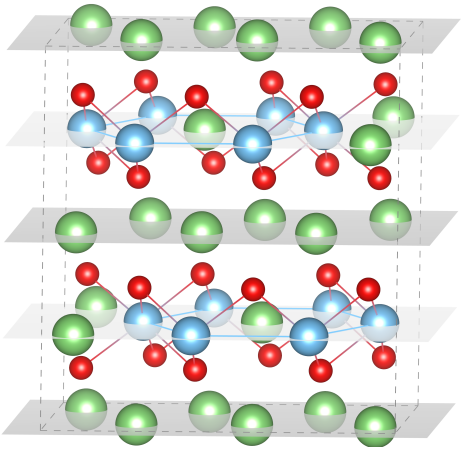

Figure 2: Unit cell of Li_2TiO_3, where green, blue and red spheres represent lithium, titanium, and oxygen atoms respectively. (The lattice constants of Li_2TiO_3 are as follows: $a = 5.06$ Å, $b = 8.79$ Å, $c = 9.75$ Å, $\beta = 100.2$ [12]). x out of page, y across, and z up.

To complement experimental studies, it is of interest to investigate the thermal conductivity of potential breeder blanket materials using computational methods. In this paper, a model is used to gain atomic-scale insight, allowing

the isolation of single effects. This allows investigation of the thermal conductivity along each spatial direction, which would be difficult to achieve from experiment.

2. Methodology

2.1. Molecular dynamics

Molecular dynamics (MD) is a classical simulation method which treats all atoms in a supercell as point particles, interacting through an interatomic empirical pair potential. A supercell is constructed from replications of the unit cells of the material being studied, and uses periodic boundary conditions to simulate an infinite crystal. MD allows the system to adopt a range of configurations as governed by Newton's laws of motion ($F = ma$) and the conditions imposed. The interatomic potential allows calculation of the forces of the particles, whose masses are known, enabling calculation of their acceleration. From these calculations, time averages of quantities of interest can be evaluated. The dynamics in the simulation are given sufficient time to reach their final configuration in the simulated conditions, thus the evaluated quantities of interest resemble real averages.

In this work, the molecular dynamics calculations are performed using the Large-scale Atomic/Molecular Massively Parallel Simulator (LAMMPS) code [14]. All simulation supercells were created using the program ATOMSK [15].

2.2. Interatomic potential

The interactions between ions were represented using an empirical potential developed by Vijayakumar *et al.* [16] based on the Born model of solids [17], and developed using previous work by Matsui and Akaogi [18] for TiO_2 polymorphs. The long-range interactions are described by a Coulombic interaction, and the short-range interactions are described using the Buckingham potential. The form of this potential can be seen in eq. 1,

$$U_{ij} = \frac{1}{4\pi\epsilon_0}\frac{q_i q_j}{r_{ij}} + A_{ij}\exp\left(-\frac{r_{ij}}{\rho_{ij}}\right) - \frac{c_{ij}}{r_{ij}^6} \tag{1}$$

where ϵ_0 is the permittivity of free space; q_i, q_j are the charges on ions (+0.549 on Li, 2.196 on Ti, and -1.098 on O) i and j; r_{ij} is the separation between two ions i and j; and $A_{ij}, \rho_{ij}, c_{ij}$ are potential parameters of Li_2TiO_3, see table 1.

Ion pair (ij)	A_{ij} (eV)	ρ_{ij} (Å)	c_{ij} (eV Å^6)
Li-Li	38533.955	0.100	0.00
Ti-Li	33089.570	0.127	0.00
Ti-Ti	31120.528	0.154	5.25
Ti-O	16957.710	0.194	12.59
Li-O	15465.549	0.167	0.00
O-O	11782.884	0.234	30.22

Table 1: Buckingham parameters of the potential used in this work [16].

As originally constructed this potential used the shell model of Dick and Overhauser[19]. However, the use of shells in MD simulations requires either the arbitrary assignment of shell masses or energy minimisation of core-shell separations at each time step, which is computationally intensive. In table 2, the values of the lattice parameters and elastic constants as produced by the empirical model employed in this work (without shells) are shown, compared to valued obtained by the empirical model when shells are included, density functional theory, and experiment. A good agreement can be seen between both empirical models with the shells on or off, and between the empirical models, DFT, and experiment, indicating the efficacy of the model used.

2.3. Non-equilibrium molecular dynamics

Thermal conductivity can be calculated using the Müller-Plathe method [21] in a non-equilibrium molecular dynamics (NEMD) simulation. The method calls for the division of the supercell into "chunks" along the direction of calculation (x, y, or z). Kinetic energy swaps are then performed between the hottest atom in the "cold chunk" and the coldest atom in the "hot chunk" (see fig. 3). This is done by the literal swap of the velocity values of the atoms. The energy cost

Property	Emp (shells off)	Emp (shells on)	DFT	Exp
a /Å	5.10	5.07	5.09	5.06
b /Å	8.85	8.80	8.83	8.79
c /Å	9.48	9.51	9.51	9.75
α /	90.00	90.00	90.00	90.00
β /	100.32	100.24	100.25	100.21
γ /	90.00	90.00	90.00	90.00
c_{11} /GPa	226.17	228.3	275.9	-
c_{12} /GPa	85.67	83.9	74.2	-
c_{13} /GPa	39.87	41.2	23.9	-
c_{15} /GPa	-5.96	8.9	22.4	-
c_{22} /GPa	219.93	223.8	269.3	-
c_{23} /GPa	40.09	40.9	24.2	-
c_{25} /GPa	15.56	11.8	25.0	-
c_{33} /GPa	116.28	123.3	209.2	-
c_{35} /GPa	2.34	2.2	2.4	-
c_{44} /GPa	34.41	37.4	57.5	-
c_{46} /GPa	14.70	11.0	23.2	-
c_{55} /GPa	33.83	37.0	56.8	-
c_{66} /GPa	68.69	71.8	103.9	-

Table 2: Table of lattice parameters and elastic constants as obtained from the empirical model with shells off (this work), empirical model with shells on [20], density functional theory [20] and experiment [12].

(Q) of performing each swap is logged as the process continues, repeating until a steady state temperature gradient (∇T) is formed. The thermal conductivity (k) can then be calculated using Fourier's law ($Q = k\nabla T$) [22].

The thermal conductivity of a material is made up of both phonon and electron contributions [23]. This method is of use in materials such as ceramics, which are dominated by phonon conductivity, which is captured by MD. However, for materials such as metals, the large electronic conductivity component would be missed using solely MD.

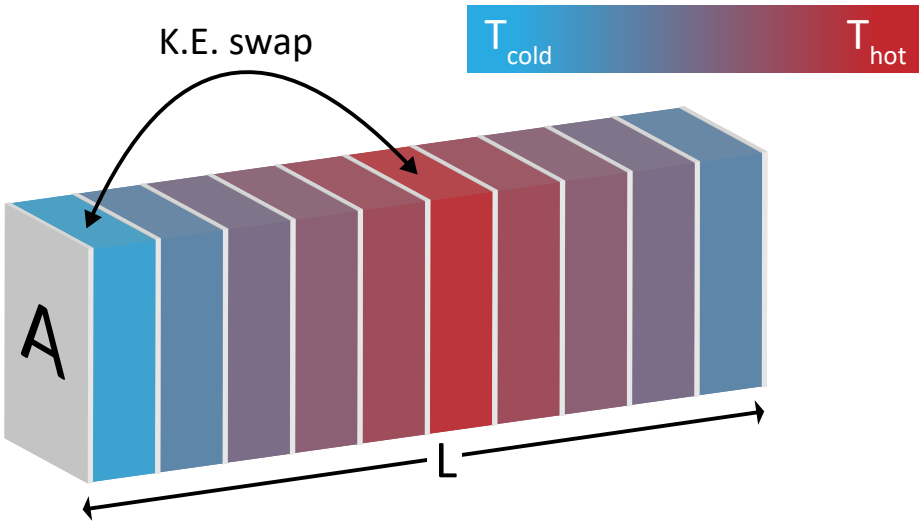

Figure 3: A supercell of length L and cross-sectional area A, in the Müller-Plathe method, where kinetic energy swaps are performed between the first chunk and centre chunk of the supercell, inducing a heat flux from the hot chunk (at temperature T_{hot}) to the cold chunk (at temperature T_{cold}).

Initially simulation supercells were equilibrated under constant pressure and temperature (NPT) conditions for 50,000 timesteps of 2 fs. Simulations employed the Nose-Hoover thermostat and barostat with relaxation times of 0.05 ps and 1.0 ps respectively. For the second part of the simulation, kinetic energy swaps were performed every 10 timesteps under constant volume and energy (NVE) conditions in the spatial direction of choice, with 20 "chunks" over which the gradient is formed. After at least 100,000 timesteps, to allow the

system to form its gradient, the temperature of each chunk is recorded every 1000 time steps, from which the thermal conductivity calculation can be made using Fourier's Law.

Fig 4 shows real temperature gradients induced in six simulations from 300 K - 1300 K. From this it can be seen that well defined temperature profiles can be achieved with this method when suitably equilibrated.

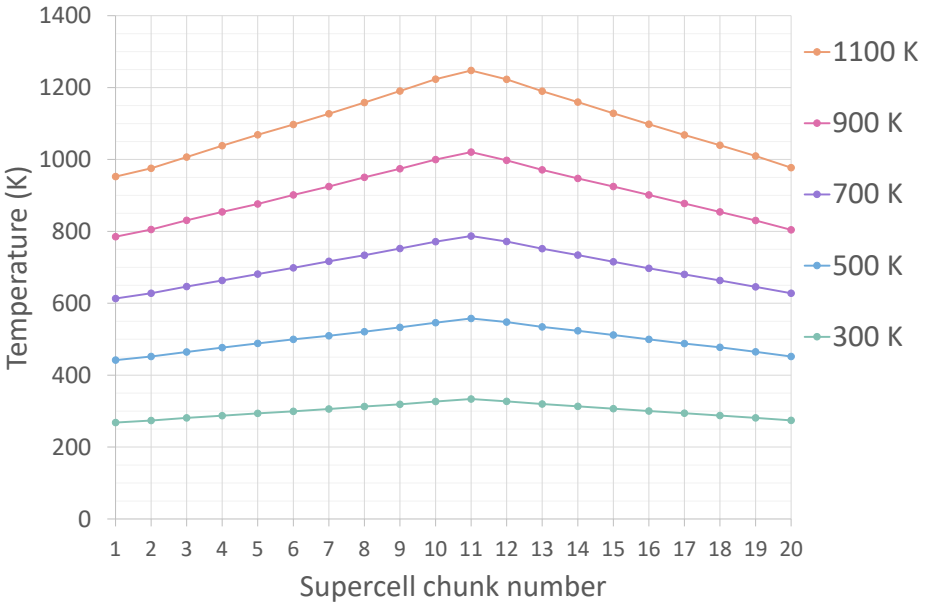

Figure 4: Temperature profiles of Li_2TiO_3, calculated for supercells of length, $L = 30$ unit cells, in the y-direction, for temperatures 300 K - 1100 K.

2.4. Extrapolation for the infinite cell

In crystalline structures, the calculated thermal conductivity exhibits a dependency on the size of the simulation supercell. This regime is known as the Casimir limit [24], and is the result of phonon scattering at the interfaces of the hot and cold chunks due to the simulation supercell length L restricting the mean free path of the phonons [25]. In an ideal case, simulations would all be run with large enough supercells to avoid this scattering effect. However, computational costs increase exponentially with increased cell size (i.e. the total number

of atoms in the simulations). It is, therefore, not computationally feasible, and so an extrapolation procedure is employed [26, 25], using the relationship,

$$\frac{1}{k} \propto \frac{1}{L} \tag{2}$$

between the thermal conductivity and supercell length.

By calculating the thermal conductivity for each temperature of interest in a range of increasing supercell lengths (L = 30, 40, 50, 100), a "true" value for the thermal conductivity can be obtained by extrapolating the calculated value to $L \to \infty$, i.e. $\frac{1}{L} \to 0$. This would be the simple intercept of a graph showing inverse thermal conductivity, $\frac{1}{k}$ against inverse supercell length, $\frac{1}{L}$. This final calculated value would be comparable to experimental single crystal results.

2.5. Minimum cell-size and convergence time-scales

To gain reliable results from simulations, there are a number of parameters that must be considered, including the cross-sectional area of the supercell and the number of time steps used to establish a converged temperature gradient. Running simulations with larger supercells (more atoms) or longer simulation run times can become very computationally expensive, requiring minimisation of cost while ensuring the accuracy of the data. Here illustrated is the testing used to determine the appropriate simulation supercell cross-section size and simulation run time.

The dependence on cross-sectional area was examined first. This was done by calculating the thermal conductivity for supercell cross-sections of 5×5, 10×10, and 20×20 unit cells. From fig. 5, the effect of increased cross-section of the simulation supercells on the temperature gradient can be seen. With a larger cross-sectional area, a gentler temperature gradient is induced. This reduces potential adverse effects such as the hot chunk passing the melting point of the material, which would create an unphysical scenario for the model. By studying these effects, a cross-sectional area of 10×10 unit cells was found to be sufficient for this work.

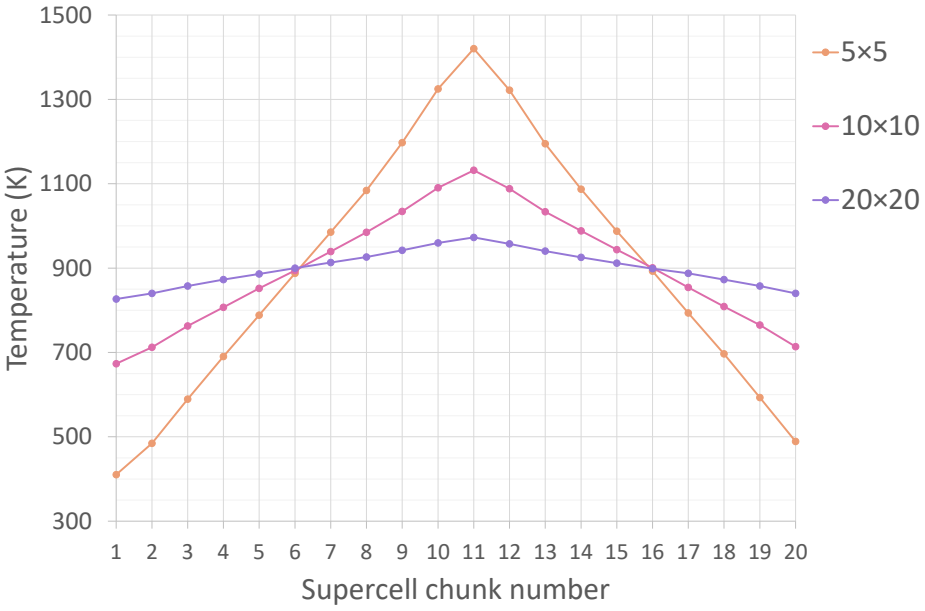

Figure 5: The temperature profiles induced using NEMD with increasing cross-section sizes of 5×5, 10×10 and 20×20 unit cells of supercell length L = 40, for the T = 900 K data set calculations along the z-direction.

The simulation length over which the kinetic energy swaps take place directly relates to the quality of the temperature profile induced, until such a point that a steady state temperature gradient is formed. To ensure this work contains converged values for the thermal conductivity, simulations were run for a range of increasing simulation lengths, until convergence was ensured in each of the three spatial directions. The difference in crystal structure of Li_2TiO_3 affected how quickly a steady state temperature gradient was induced in each direction. Most notably the z direction requires significantly more time on average (500 ps) than x or y (200 ps) to achieve convergence, see fig. 6. Final simulations along x and y were run for 200 ps and along z for 500 ps. There is notably also a positive correlation between the length, L, of the supercell and the time required for convergence. To maximise the use of computational resources this was accounted for to ensure all data produced in this work is well converged by giving all the largest $L = 100$ simulations twice as long to run (i.e. simulations

along x and y were run for 500 ps and along z for 1000 ps).

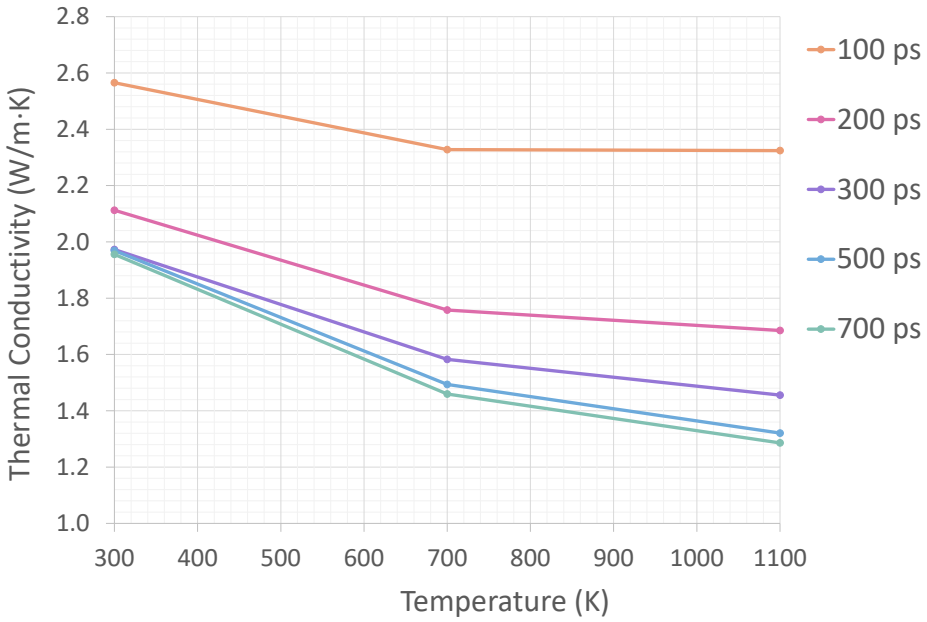

Figure 6: Plot of the calculated thermal conductivity along z, as a function of temperature over a range of simulation lengths (100 ps, 200 ps, 500 ps and 700 ps).

3. Results and discussion

Plotted in fig. 7 is the thermal conductivity as a function of the inverse of the supercell length in the direction of interest, at a series of temperatures. The straight line trends obtained enable the extrapolation of the thermal conductivity in each direction, to represent the infinite cell.

The extrapolation was performed for all three spatial directions, allowing for calculation of the thermal conductivity in x, y, and z to be displayed in fig. 8. From this figure the anisotropy of the thermal conductivity of Li_2TiO_3 can be clearly observed. The x, and y thermal conductivities remain similar to each other, while the z-direction thermal conductivity is markedly lower than both. The origin of this anisotropy is due to the crystal structure of the host material. The crystal structure of Li_2TiO_3 along z differs greatly from the more

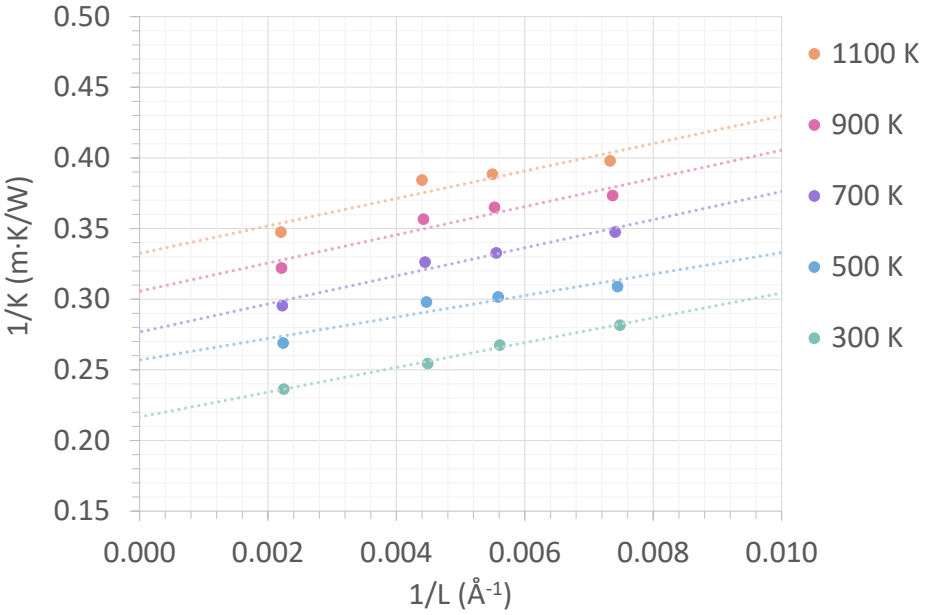

Figure 7: The inverse thermal conductivity in y as a function of inverse supercell-length L, the intercept of which is the thermal conductivity of the infinite cell in y.

similar structures of x and y. There is very clear bonding in the xy-plane but not between the layers along z (the lithium L_6 layer, the oxygen O_6 layer and the mixed cation layer of Li_2Ti_4, see. fig. 2). The difference in bonding along z appears to inhibit thermal transport, and thus lower the thermal conductivity. This may be due to increased phonon scattering along the path of the bonding in z. Kataoka *et al.* measured the thermal conductivity of a single crystal, finding the thermal conductivity in z as being 0.93 W/(m·K) at 294 K, that is, much lower than the reported value for Li_2TiO_3, implying strong anisotropy [12]. This observed lower thermal conductivity may also account for why simulations along z required longer to achieve a steady state temperature gradient, as was found when checking the convergence of simulations (section 2.5).

Alongside these data, the average (arithmetic mean) of the extrapolated thermal conductivity of Li_2TiO_3 is shown. These are the values most comparable to experiment, where the grains of Li_2TiO_3 are randomly oriented. The

overall trend in the thermal conductivity is that it decreases with increased temperature, as is the case for most materials [23]. It can also be seen from figure 8 how much the lower thermal conductivity along z lowers the average thermal conductivity, highlighting the magnitude of its influence.

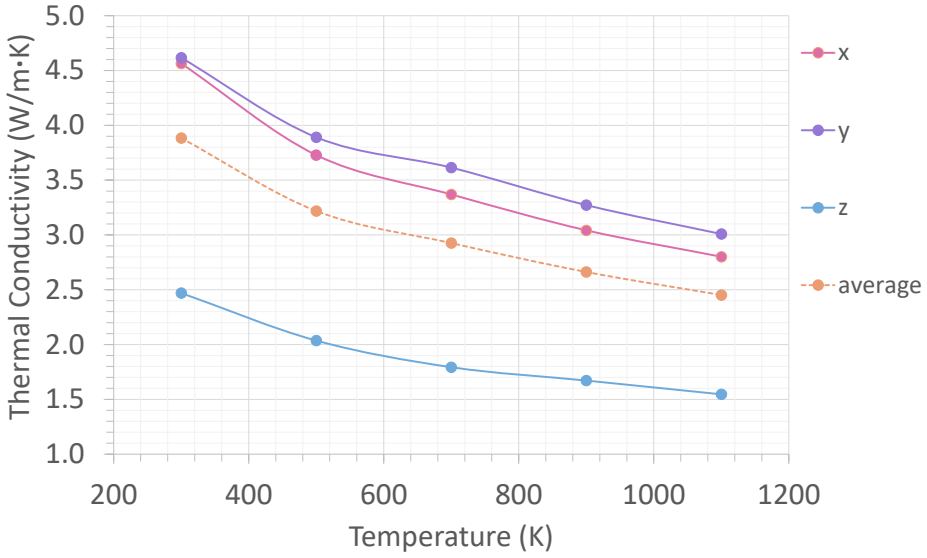

Figure 8: The extrapolated thermal conductivity in x, y, and z, along with the average thermal conductivity.

There have been a number of studies of the thermal conductivity of Li_2TiO_3. The data show considerable variation depending on the size of the pebbles, grain size, density of the material, and the particular chemical composition chosen for study. A summary of the existing data for the thermal conductivity of Li_2TiO_3 has been reproduced in fig. 9. It is hard to draw many conclusions based on the data presented in fig 9. Davis and Haasz [27], and Saito *et al.* [28] investigate the thermal conductivity of pebbles of Li_2TiO_3, similar to those that will be used in a breeder blanket design. Saito *et al.* used 8 mm diameter by 2 mm thickness pellets of three theoretical densities (TD), here plotted for comparison is 83 % TD. Hoshino *et al.* [29] investigates non-stoichiometric compositions of Li_2TiO_3. In fig 9 it is the thermal conductivity of $95Li_2TiO_3$, i.e. where the molecular ratio of Li_2O over TiO_2 is 0.95 (lithium deficient), that

is plotted. One might anticipate that the non-stoichiometric material would have a lower thermal conductivity, due to the introduction of point defects which act as phonon scattering centres. However, Hoshino *et al.* found the thermal conductivity to be higher than for the stoichiometric Li_2TiO_3 found by Saito *et al.*. This highlights one example of the complex nature of Li_2TiO_3, and the clear need for further study. Another feature seen in the experimental data from Saito *et al.* and Davis Haasz is a small increase in the thermal conductivity at high temperature. Though the phonon contribution to the thermal conductivity (as calculated in this work) would be anticipated to drop with temperature, the photon conductivity can exhibit a slight increase [30]. This change can be significant, however, it depends on the particular composition of the sample. It may be that the data of Saito *et al.* and Davis & Haasz is indicating that there is increased photon conductivity at high temperature.

The average thermal conductivity calculated in this work can now be compared to experimental results as seen in fig. 9. The values for thermal conductivity found in this work are consistently higher than that shown in experiment. This is to be expected, as the simulations of this work do not include any of the defects found in real Li_2TiO_3, such as grain boundaries, where phonon scattering lowers the thermal conductivity. Overall the trend of the thermal conductivity follows the experimental data, with the exception of experiments where the thermal conductivity was found to decrease initially and then rise again with increased temperature, which could originate from impurities in the crystal structure not captured in the present simulations. This could suggest that this distinct behaviour is not inherent to the pure crystal structure, which would be expected to be observed in this work.

4. Conclusion

This work has examined the thermal conductivity of Li_2TiO_3 and highlighted how the complex underlying crystal structure results in highly anisotropic heat transfer in the material. The overall thermal conductivity of the material is pre-

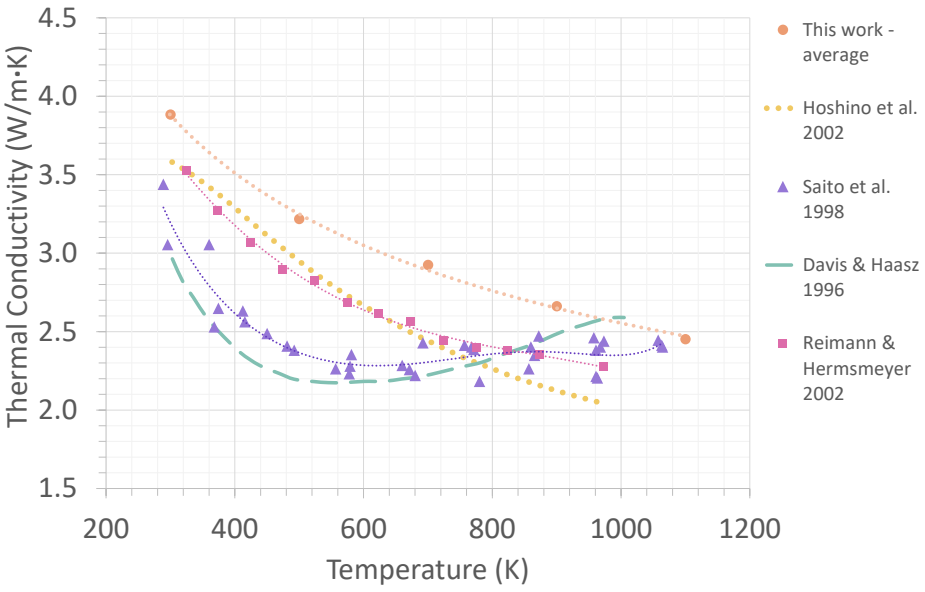

Figure 9: The extrapolated thermal conductivity compared with current experimental data [27, 28, 29, 31].

dicted to be slightly higher than experimental observations, but this is expected as the current model neglects the impact of defects (including grain boundaries) and impurities. The results suggest that thermal conductivity in the z direction (the direction in which the crystal structure alternates between Li, O and $LiTi_2$ (111) planes) is roughly half that predicted in the x and y directions where planes are homogeneous. This interesting characteristic could potentially be exploited using methods of creating breeder blankets where the crystal structure of all grains of Li_2TiO_3 are favourably aligned to give the blanket a higher thermal conductivity than the average for the material. Current solid breeder blanket designs utilising pebbles do not make use of selectively orienting crystal structure.

With the foundation of the calculated thermal conductivities of the perfect crystal, further work will proceed with the effect of defects on the thermal conductivity of Li_2TiO_3. In particular, Li_2TiO_3 is typically manufactured for breeding applications with a certain level of open porosity (10-12% [32]). This

porosity is required in order to allow tritium to diffuse out of the material (so that it can be extracted and fed back into the fusion fuel cycle) and prevent it from becoming trapped in, for example, voids created by neutron damage. However, pores will act as scattering centres, reducing thermal conductivity, and thus impacting thermal performance. The effect must be properly understood as part of the engineering design process of breeder blankets. This will achieved in follow-on work in the first instance by investigating non-stoichiometric Li_2TiO_3. Furthermore, the blanket module will experience high neutron irradiation fluxes, leading to the inevitable formation of defects in the breeding material. The effect of these defects on the thermal conductivity must also be studied in order to make predictions on the lifetime of the breeder blanket in a fusion reactor.

Acknowledgements

This work has been carried out within the framework of the EUROfusion consortium and has received funding from the Euratom research and training programme 2014-2018 and 2019-2020 under grant agreement No 633053. The views and opinions expressed herein do not necessarily reflect those of the European Commission.

MRG acknowledges funding from the RCUK [grant number EP/T012250/1].

This work was performed using resources provided by the Cambridge Service for Data Driven Discovery (CSD3) operated by the University of Cambridge Research Computing Service (www.csd3.cam.ac.uk), provided by Dell EMC and Intel using Tier-2 funding from the Engineering and Physical Sciences Research Council (capital grant EP/P020259/1), and DiRAC funding from the Science and Technology Facilities Council (www.dirac.ac.uk).

Via our membership of the UK's HEC Materials Chemistry Consortium, which is funded by EPSRC (EP/L000202, EP/R029431), this work used the ARCHER UK National Supercomputing Service (http://www.archer.ac.uk).

References

[1] R. L. Murray, K. E. Holbert, Nuclear Energy - An Introduction to the Concepts, Systems, and Applications of Nuclear Processes (7th Edition), Elsevier, 2015.

[2] G. Federici, L. Boccaccini, F. Cismondi, M. Gasparotto, Y. Poitevin, I. Ricapito, An overview of the EU breeding blanket design strategy as an integral part of the DEMO design effort, Fusion Engineering and Design 141 (2019) 30 – 42.

[3] T. Ihli, T. Basu, L. Giancarli, S. Konishi, S. Malang, F. Najmabadi, S. Nishio, A. Raffray, C. Rao, A. Sagara, Y. Wu, Review of blanket designs for advanced fusion reactors, Fusion Engineering and Design 83 (7) (2008) 912 – 919, proceedings of the Eight International Symposium of Fusion Nuclear Technology.

[4] G. Federici, W. Biel, M. Gilbert, R. Kemp, N. Taylor, R. Wenninger, European DEMO design strategy and consequences for materials, Nuclear Fusion 57 (9) (2017) 092002.

[5] L. Giancarli, M. Dalle Donne, W. Dietz, Status of the European breeding blanket technology, Fusion Engineering and Design 36 (1) (1997) 57 – 74.

[6] R. Knitter, P. Chaudhuri, Y. Feng, T. Hoshino, I.-K. Yu, Recent developments of solid breeder fabrication, Journal of Nuclear Materials 442 (1, Supplement 1) (2013) S420 – S424, fifteenth International Conference on Fusion Reactor Materials.

[7] S. Konishi, M. Enoeda, M. Nakamichi, T. Hoshino, A. Ying, S. Sharafat, S. Smolentsev, Functional materials for breeding blankets—status and developments, Nuclear Fusion 57 (9) (2017) 092014.

[8] C. Alvani, S. Casadio, A. D. Bartolomeo, J. D. Lulewicz, N. Roux, Li_2TiO_3 pebbles reprocessing, recovery of ^6Li as Li_2CO_3, Journal of Nuclear Materials 307-311 (2002) 837 – 841.

[9] L. Giancarli, V. Barabash, D. Campbell, S. Chiocchio, J.-J. Cordier, A. Dammann, G. Dell'Orco, J. Elbez-Uzan, J. Fourneron, J. Friconneau, M. Gasparotto, M. Iseli, C.-Y. Jung, B.-Y. Kim, D. Lazarov, B. Levesy, M. Loughlin, M. Merola, J.-C. Nevière, R. Pascal, W. Ring, I. Schneiderova, S. Willms, A. Siarras, W. Shu, J. Snipes, J. van der Laan, Progress and challenges of the ITER TBM program from the IO perspective, Fusion Engineering and Design 109-111 (2016) 1491 – 1497, Proceedings of the 12th International Symposium on Fusion Nuclear Technology-12 (ISFNT-12).

[10] H. Kleykamp, Phase equilibria in the Li–Ti–O system and physical properties of Li_2TiO_3, Fusion Engineering and Design 61-62 (2002) 361 – 366.

[11] G. Lang, Die kristallstruktur einiger vertreter der verbindungs-klasse $Me^I_2Me^{IV}O_3$ als beitrag zur aufklrung der ordnungsphase von Li_2TiO_3, Zeitschrift für anorganische und allgemeine Chemie 276 (1954) 77–94.

[12] K. Kataoka, Y. Takahashi, N. Kijima, H. Nagai, J. Akimoto, Y. Idemoto, K. Ohshima, Crystal growth and structure refinement of monoclinic Li_2TiO_3, Materials Research Bulletin 44 (1) (2009) 168 – 172.

[13] K. Azuma, C. Dover, D. C. Grinter, R. Grau-Crespo, N. Almora-Barrios, G. Thornton, T. Oda, S. Tanaka, Scanning tunneling microscopy and molecular dynamics study of the Li_2TiO_3 (001) surface, The Journal of Physical Chemistry C 117 (10) (2013) 5126–5131.

[14] S. Plimpton, Fast parallel algorithms for short-range molecular dynamics, J Comp Phys 117 (1995) 1–19.
URL `http://lammps.sandia.gov`

[15] P. Hirel, Atomsk: A tool for manipulating and converting atomic data files, Computer Physics Communications 197 (2015) 212 – 219.

[16] M. Vijayakumar, S. Kerisit, Z. Yang, G. L. Graff, J. Liu, J. A. Sears, S. D. Burton, K. M. Rosso, J. Hu, Combined 6,7 Li NMR and molecular dynam-

ics study of Li diffusion in Li_2TiO_3, The Journal of Physical Chemistry C 113 (46) (2009) 20108–20116.

[17] M. Born, K. Huang, Dynamical Theory of Crystal Lattices, International series of monographs on physics, Oxford: Clarendon Press, 1954.

[18] M. Matsui, M. Akaogi, Molecular dynamics simulation of the structural and physical properties of the four polymorphs of TiO_2, Molecular Simulation 6 (4-6) (1991) 239–244.

[19] B. G. Dick, A. W. Overhauser, Theory of the dielectric constants of alkali halide crystals, Physical Review 112 (1958) 90 – 103.

[20] S. T. Murphy, P. Zeller, A. Chartier, L. Van Brutzel, Atomistic simulation of the structural, thermodynamic, and elastic properties of Li_2TiO_3, The Journal of Physical Chemistry C 115 (44) (2011) 21874–21881.

[21] F. Müller-Plathe, A simple nonequilibrium molecular dynamics method for calculating the thermal conductivity, The Journal of Chemical Physics 106 (14) (1997) 6082–6085.

[22] J. Fourier, The analytical theory of heat, Cambridge University Press, 1878.

[23] D. W. Hahn, Heat conduction, 3rd Edition, Wiley, Hoboken, N.J., 2012.

[24] H. Casimir, Note on the conduction of heat in crystals, Physica 5 (6) (1938) 495 – 500.

[25] C. Oligschleger, J. C. Schön, Simulation of thermal conductivity and heat transport in solids, Phys. Rev. B 59 (1999) 4125–4133.

[26] P. K. Schelling, S. R. Phillpot, P. Keblinski, Comparison of atomic-level simulation methods for computing thermal conductivity, Phys. Rev. B 65 (2002) 144306.

[27] J. Davis, A. A. Haasz, Thermal diffusivity/conductivity of AECL Li_2TiO_3 ceramic, Journal of Nuclear Materials 232 (1996) 65–68.

[28] S. Saito, K. Tsuchiya, H. Kawamura, T. Terai, S. Tanaka, Density dependence on thermal properties of Li_2TiO_3 pellets, Journal of Nuclear Materials 253 (1998) 213–218.

[29] T. Hoshino, M. Dokiya, T. Terai, Y. Takahashi, M. Yamawaki, Non-stoichiometry and its effect on thermal properties of Li_2TiO_3, Fusion Engineering and Design 61-62 (2002) 353–360.

[30] M. Zhao, X. Ren, W. Pan, Mechanical and thermal properties of simultaneously substituted pyrochlore compounds $(ca_2nb_2o_7)_x(gd_2zr_2o_7)_{1x}$, Journal of the European Ceramic Society 35 (3) (2015) 1055–1061.

[31] J. Reimann, S. Hermsmeyer, Thermal conductivity of compressed ceramic breeder pebble beds, Fusion Engineering and Design 61-62 (2002) 345–351.

[32] M. Xiang, Y. Zhang, Zhang, C. Yun Wang, Y. Yu, Effect of the fabrication process of ceramic pebbles on the porosity of Li_2TiO_3 tritium breeder, Journal of Fusion Energy 34 (2015) 1423–1432.